

# Magneto-Mechanical Bilayer Metamaterial with Global Area-Preserving Density Tunability for Acoustic Wave Regulation

Jay Sim, Shuai Wu, Jize Dai, and Ruike Renee Zhao\*

2D metamaterials have immense potential in acoustics, optics, and electromagnetic applications due to their unique properties and ability to conform to curved substrates. Active metamaterials have attracted significant research attention because of their on-demand tunable properties and performances through shape reconfigurations. 2D active metamaterials often achieve active properties through internal structural deformations, which lead to changes in overall dimensions. This demands corresponding alterations of the conforming substrate, or the metamaterial fails to provide complete area coverage, which can be a significant limitation for their practical applications. To date, achieving area-preserving active 2D metamaterials with distinct shape reconfigurations remains a prominent challenge. In this paper, magneto-mechanical bilayer metamaterials are presented that demonstrate area density tunability with area-preserving capability. The bilayer metamaterials consist of two arrays of magnetic soft materials with distinct magnetization distributions. Under a magnetic field, each layer behaves differently, which allows the metamaterial to reconfigure its shape into multiple modes and to significantly tune its area density without changing its overall dimensions. The area-preserving multimodal shape reconfigurations are further exploited as active acoustic wave regulators to tune bandgaps and wave propagations. The bilayer approach thus provides a new concept for the design of area-preserving active metamaterials for broader applications.

Acoustic 2D metamaterials can also be engineered to filter,<sup>[12–14]</sup> isolate,<sup>[15,16]</sup> cloak,<sup>[17–19]</sup> regulate wave transmission,<sup>[20–22]</sup> as well as absorb,<sup>[23,24]</sup> or steer acoustic waves.<sup>[25–27]</sup>


In general, the properties of metamaterials are determined by their geometry.<sup>[28]</sup> Conventional metamaterials have fixed unit cell geometries and, accordingly, fixed properties, which limits their applicability. In response, active metamaterials have emerged, which can transform between preprogrammed shapes when subjected to external stimuli, such as mechanical loads,<sup>[29–32]</sup> heat,<sup>[33–36]</sup> electrical currents,<sup>[37–40]</sup> or magnetic fields.<sup>[41–44]</sup> These shape transformations often involve internal deformations of the unit cells, which also change the area density and the overall dimensions of the metamaterial. However, a 2D metamaterial covers a specific area. If its overall dimensions change dramatically during actuation, the 2D metamaterial would either demand the corresponding alterations of the substrate it covers or fail to provide complete area coverage, which could impose significant limitations for practical applications.

In this paper, we present a new 2D metamaterial design strategy that can significantly change the area density while maintaining the overall area through a novel bilayer concept. Here, the 2D metamaterials are made of hard-magnetic soft active materials (hm-SAM),<sup>[45]</sup> which have a soft elastomer matrix embedded with hard magnetic particles. The material can provide untethered, fast, and reversible actuation by a remotely applied magnetic field.<sup>[46–49]</sup> The square-shaped unit cell of the 2D metamaterial is first designed with a preprogrammed magnetization distribution that can induce contraction for area density change under an external magnetic field. When we overlay two arrays in specific arrangements, they form an integrated material with strong interfacial adhesion because of the magnetic attraction. Under an external magnetic field, only one layer significantly contracts to provide the area density change; the other maintains the overall dimensions of the 2D metamaterial, a process otherwise unobtainable in a single layer setting. In addition, the separate layer actuation increases the number of unique shape reconfigurations and, therefore, acoustic properties. Based on this concept, we demonstrate bilayer metamaterial designs with different

## 1. Introduction

Metamaterials are manmade materials with a periodic structure comprised of unit cells and are engineered to exhibit extraordinary properties<sup>[1]</sup> derived from their geometry rather than the material composition.<sup>[2]</sup> 2D metamaterials consist of repeating periodic 2D unit cells and are commonly designed to conform to flat or curved substrates for various applications. 2D metamaterials in optics can be designed to scatter,<sup>[3]</sup> refract,<sup>[4]</sup> and modulate the intensity of<sup>[5,6]</sup> light, creating new methods for light manipulation. Similarly, electromagnetic waves are scattered into specific shapes,<sup>[7,8]</sup> cloaked,<sup>[8]</sup> steered,<sup>[9,10]</sup> or filtered.<sup>[11]</sup>

J. Sim, S. Wu, J. Dai, R. R. Zhao  
Department of Mechanical Engineering  
Stanford University  
Stanford, CA 94305, USA  
E-mail: rrzhao@stanford.edu

 The ORCID identification number(s) for the author(s) of this article can be found under <https://doi.org/10.1002/adma.202303541>

DOI: 10.1002/adma.202303541

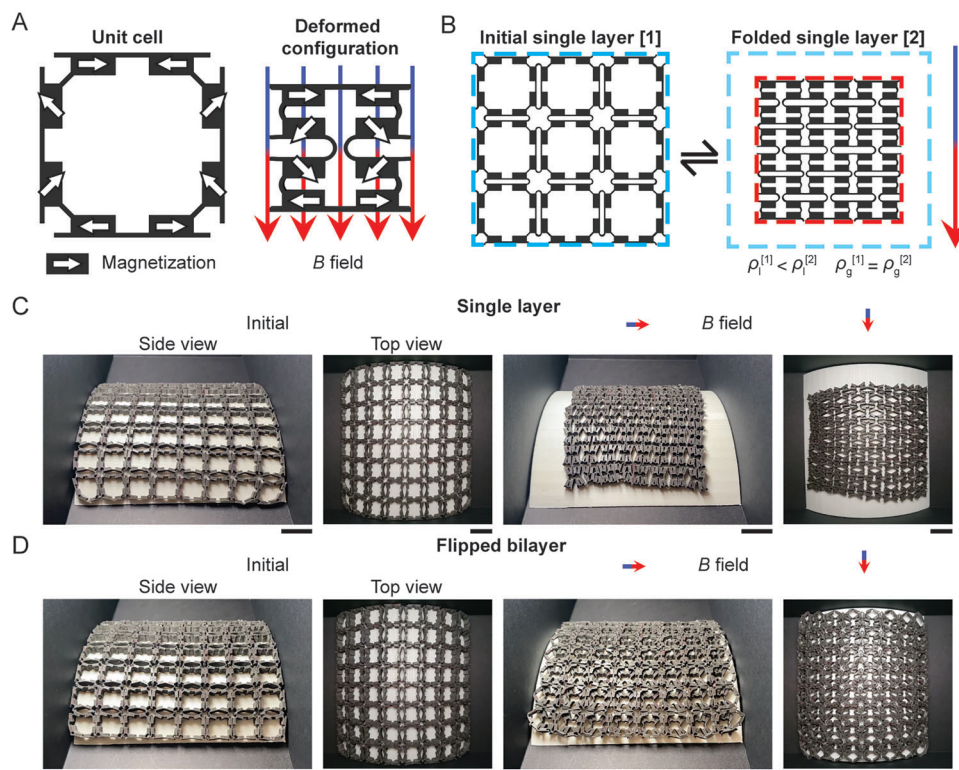


**Figure 1.** Magneto-mechanical single layer metamaterial with area-changing actuation and bilayer metamaterial for area-preserving actuation. A) Magnetization distribution and actuation of a unit cell. B) A single layer metamaterial and its actuation to the folded mode, with the initial and deformed configuration areas denoted by the dashed blue and red boxes, respectively. The global area density,  $\rho_g$ , is constant during actuation but the local area density,  $\rho_l$ , increases. C) The single layer metamaterial conforms to a curved substrate with incomplete area coverage after actuation. D) The bilayer metamaterial conforms to a curved substrate with complete area coverage throughout actuation. Scale bars: 20 mm.

assembling strategies, including a flipping strategy, distributed patches, and an offset strategy. Their corresponding wave regulation performances, bandgap and waveguide, are also explored. Parametric studies for the flip-arranged bilayer explore how the bilayer material composition and layer thickness ratio can be programmed to tune acoustic bandgaps. The ability of the bilayer metamaterial to greatly change its area density while retaining constant overall dimensions thus provides a new strategy for designing highly tunable area-preserving conformal acoustic regulators for practical applications.

## 2. Results and Discussion

### 2.1. Actuation and Performance of Single Layer and Flipped Bilayer Metamaterials

As shown in **Figure 1A**, the square-shaped unit cell design in this work consists of eight rectangular blocks connected with thin hinges. Both hinges and blocks are hm-SAMs and are fabricated using casting methods. Further information on the dimensions and fabrication method can be found in the experimental methods and Figures S1 and S2 (Supporting Information). The unit cells are magnetized with a predetermined magnetization distribution, as denoted by the white arrows, to enable area contraction for density change under an external magnetic field. The upper and lower blocks are magnetized along the block length

in alternating directions; the side blocks are magnetized diagonally at  $45^\circ$ . Here, the magnetization directions are carefully designed to provide special actuation. When a downward magnetic field is applied, the block's magnetization tends to align with the magnetic field due to the generated torque,  $\mathbf{T} = V \mathbf{M} \times \mathbf{B}$ , where  $V$  and  $\mathbf{M}$  are the volume and magnetic moment density of the blocks, and  $\mathbf{B}$  is the magnetic field. For the upper and lower blocks, the magnetization is initially  $90^\circ$  to the magnetic field. As the block rotates, the torque decreases from its maximum value. For the side blocks, the magnetization is initially  $135^\circ$  to the magnetic field. The corresponding torque is initially smaller than that of the upper and lower blocks but increases as the side blocks rotate by  $45^\circ$  and then starts to decrease. As a result, the unit cell tries to deform into a cross shape first and then packs into a much smaller rectangular shape. The unit cell is reconfigurable, and in the absence of a magnetic field, it reverts to the initial mode. Individual unit cells can be connected to create a single layer array, as illustrated in **Figure 1B**. Under a downward magnetic field, the single layer metamaterial actuates like an individual unit cell and deforms into the folded mode. In the absence of a magnetic field, the metamaterial likewise recovers to the initial mode. The total area of the single layer in the initial configuration is marked by the dashed blue box, while the deformed configuration is marked by the dashed red box (in the rest of the paper, we will use the dashed blue box for the initial configuration and the dashed red box for the deformed

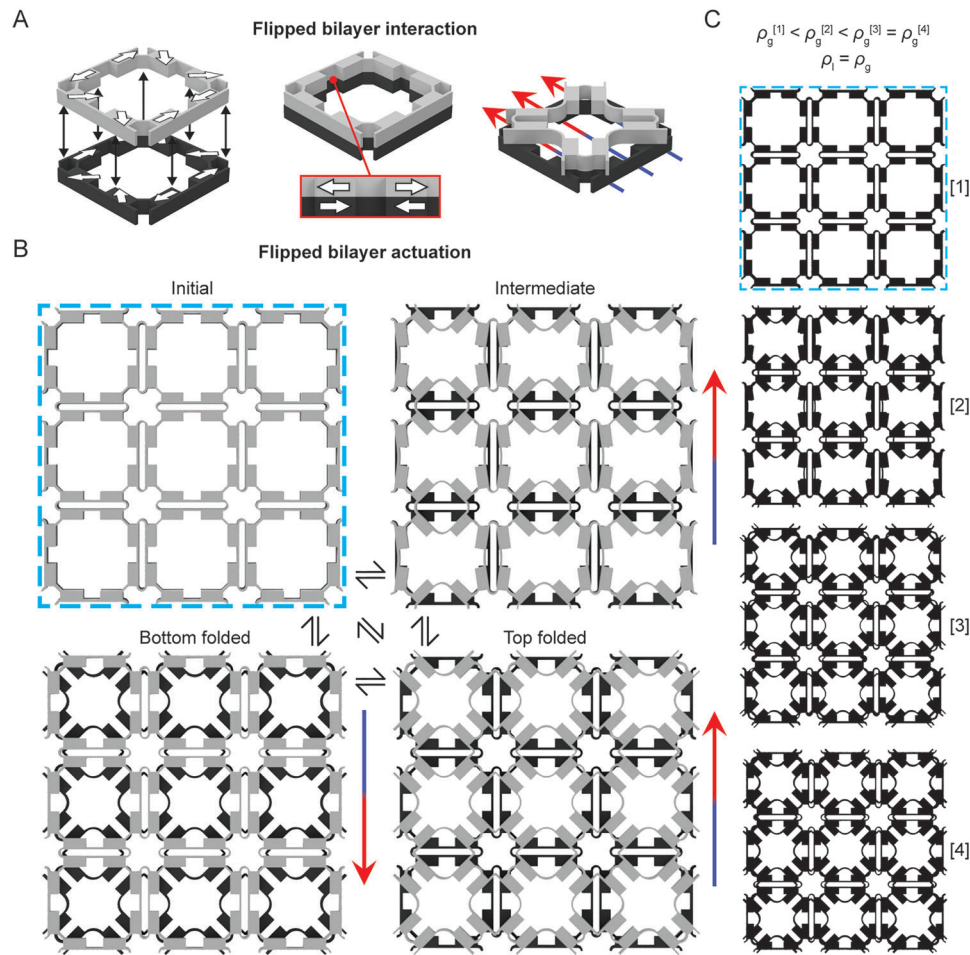


**Figure 2.** Flipped bilayer metamaterial. A) Magnetic interaction between two unit cells arranged in a flipped bilayer and their actuation. B) A  $3 \times 3$  flipped bilayer and its magnetic actuation. There are four modes: initial, intermediate, top folded, and bottom folded. C) Comparison of the area densities for the four flipped bilayer modes. Because  $A_{\text{initial}}$  and  $A_{\text{deform}}$  are the same, their global and local area densities are the same. Area densities increase from the initial mode to the intermediate mode and then the top folded mode. There is no change in area densities between the top folded and bottom folded modes.

configuration). We also define two types of area densities,  $\rho_g$  and  $\rho_l$ , as the global area density and the local area density, which are the 2D material's surface area of the metamaterial ( $A_{\text{meta}}$ ) divided by the area of the initial configuration ( $A_{\text{initial}}$ ) and the total area of the deformed mode ( $A_{\text{deform}}$ ), respectively. During the actuation of the single layer metamaterial, although its  $\rho_l$  significantly increases from 0.34 to 0.69 when the unit cells turn into a compact shape, its  $\rho_g$  remains constant as there is no addition to the material surface area. Thus, there is a region surrounding the deformed 2D metamaterial without material coverage, implying the metamaterial must reduce its size to increase its local area density. This is a common dilemma faced by conventional active 2D metamaterial designs. It should also be noted that under an upward magnetic field, the unit cell expands.<sup>[50]</sup> However, this expansion is suppressed in the array by the contact between neighboring unit cells. Therefore, under an upward field, there is no obvious area density change. Figure 1C depicts the challenges in developing an area-preserving 2D metamaterial. Here, the single layer magneto-mechanical metamaterial conforms to a curved substrate. When there is no magnetic field, it covers the entirety

of the substrate. But when a magnetic field is applied and the 2D metamaterial undergoes actuation, the single layer metamaterial rapidly contracts, leaving a significant area of the substrate uncovered. However, the magneto-mechanical 2D metamaterial demonstrated in this work, for example, the bilayer in a flipped arrangement (Figure 1D), enables global area preservation during reconfiguration, namely maintaining the substrate coverage under the applied magnetic field. The 2D metamaterials covering the curved substrate are found in Video S1 (Supporting Information).

In this work, we use different ways to overlay two array layers into a bilayer metamaterial to effectively tune its area density while preserving its global dimension. As illustrated in Figure 2A, a flipped unit cell is placed on top of the original unit. Since each block in the top unit cell has a reversed, or flipped, magnetization direction than that of the corresponding block in the bottom unit cell, there is a strong magnetic attraction and adhesion at the interface of the layers. In addition, because the unit cells have flipped magnetization distributions, only one layer can fold, or actuate, and the other layer does not change its shape,

regardless of the direction of the applied magnetic field. This separately controlled actuation is the key design concept in the flipped bilayer, as shown in Figure 2B. In the initial mode, where there is no applied magnetic field, the flipped bilayer metamaterial has the same configuration as the single layer. Under an upward magnetic field, only the upper and lower blocks of the top layer detach from the bottom layer and fold, while the side blocks are largely undeformed. This mode is referred to as the intermediate mode and occurs because of the magnetization design of the unit cell and the attractive interaction between the two layers. In this top layer folded mode, the bottom layer remains unfolded, and the strong magnetic attraction between the top and bottom arrays constrains the overall dimension change of the top layer while allowing its local shape reconfiguration. As discussed above, the magnetizations of the upper and lower blocks are perpendicular to the applied field to provide the largest torques. In comparison, the angle between the magnetizations in the side blocks and the magnetic field is  $135^\circ$ , which leads to smaller torques. Therefore, the upper and lower blocks break the constraints from the magnetic interactions between two layers and actuate first, leading to the intermediate mode. When the upward field increases further, the torques on the side blocks become sufficient to overcome the magnetic interactions. Thus, all the blocks are fully actuated, and the top layer reconfigures into a cross shape, which is the top folded mode. Due to the unactuated bottom layer, there is no obvious overall dimension change in the metamaterial. Under a downward magnetic field, the actuation reverses, where the bottom layer folds and the top layer remains unfolded. Again, the separate actuation of layers provides folding and large shape deformation while preserving the global dimension of the 2D metamaterial. In addition, when the magnetic field's direction and amplitude are changed, the bilayer metamaterial will change its shape deformation mode accordingly. Figure 2C shows the area density change of the flipped bilayer during the magnetic actuation. In the flipped bilayer case, the blue and red boxes have the same area. Therefore, the global area density is the same as the local area density. We term the area density of the initial mode as  $\rho_1$ . In the initial mode, the 2D area of the material is the same as a single layer. For the area density of the intermediate mode, or  $\rho_2$ , the top layer partially folds, increasing the flipped bilayer's material area, and  $\rho_2 > \rho_1$ . In the top folded mode, because the remaining parts of the top layer fold inward, increasing the material area further, its area density,  $\rho_3$ , is larger than  $\rho_2$ . For the bottom folded mode, since it is a reversed top folded mode, its area density,  $\rho_4$  is the same as  $\rho_3$ .

## 2.2. Flipped Bilayer

To demonstrate the bilayer metamaterial's superior performance, we first look at the actuation of the single layer metamaterial. Figure 3A shows the fabricated single layer using 2 mm thick unit cells with 25 vol.% NdFeB particles (see Figure S3, Supporting Information, for material characterizations). There are 64 unit cells arranged in an  $8 \times 8$  grid. The single layer metamaterial is placed between a pair of Helmholtz coils, which provide a single-axis homogeneous magnetic field (see Figure S4, Supporting Information, for the experimental setup). In the initial mode, the vertical blocks in the single layer metamaterial exhibit negligible folding

due to small repulsive forces between unit cells. A downward 68 mT magnetic field folds the material into the folded mode with significant global dimension reduction (Video S2, Supporting Information). Figure 3B examines the area density change of the single layer metamaterial with the applied downward magnetic field (see Figure S5, Supporting Information, for the area density change of the metamaterial in an upward field). In the initial mode, both the global and local area densities are 0.34. The local density increases drastically to 0.69 under an increasing downward magnetic field. However, the global density is constant during actuation because there is no material addition or reduction. The acoustic transmission versus frequency curves of the single layer metamaterial in the folded and deployed modes can be found in Figure S6 (Supporting Information). Based on the concept of the flipped bilayer designs shown in Figure 2, we next present the experimental results to show how the flipped bilayer can achieve area-preserving actuation for significant density change and acoustic wave regulation. Figure 3C shows the schematic and experimental actuation (Video S3, Supporting Information) of the unit cells in the four modes of the flipped bilayer metamaterial: initial, intermediate, top folded, and bottom folded. The flipped bilayer consists of two layers of 64 unit cells each, arranged in  $8 \times 8$  grids with no offset in horizontal or vertical directions. The top layer is 2 mm thick with 25 vol.% Nd-FeB particles, and the bottom is 4 mm thick with 30 vol.% Nd-FeB particles. The difference in thickness and particle volume fraction of the layers allows for wider tunable acoustic performance when each layer is actuated separately. Figure 3D shows the global and local area densities versus the upward magnetic field for the flipped bilayer. Since this bilayer preserves the global dimensions during actuation, its local area density is expected to always be the same as the global area density. At 0 mT, the flipped bilayer has an area density of 0.34, which is the same as the area density of the single layer. When an upward magnetic field is applied, the global area density closely follows the local area density during actuation. At an upward 68 mT magnetic field, the global and local area densities are 0.64 and 0.67, respectively, showing great agreement. Figure S7 (Supporting Information) shows more information on the area densities of the flipped bilayer. Figure 3E depicts the flipped bilayer magnetic actuation. All modes can switch to all other modes directly, and the reconfiguration of the metamaterial depends only on the direction and amplitude of the applied magnetic field. An upward magnetic field of 36 mT is applied to actuate the 2D metamaterial into the intermediate mode, where the upper and lower blocks of the unit cells in the top layer fold inward. But while the top layer is actuated, the bottom layer does not fold because its unit cells are programmed with reversed magnetizations. This independent actuation of the top layer allows for distinct shape deformation with negligible overall dimension change, as shown by the unchanged dashed blue box. The field is then increased to 68 mT upward to achieve the top-folded mode, which has the highest area density. The blocks in the top layer fold inward to create a cross shape, and the bottom layer remains undeformed. Lastly, the 2D metamaterial achieves the bottom folded mode under a downward field of 68 mT. The flipped bilayer displays four distinct modes that can be controlled by adjusting the direction and magnitude of the applied magnetic field. Note that the actuation in the intermediate top mode is not completely uniform,

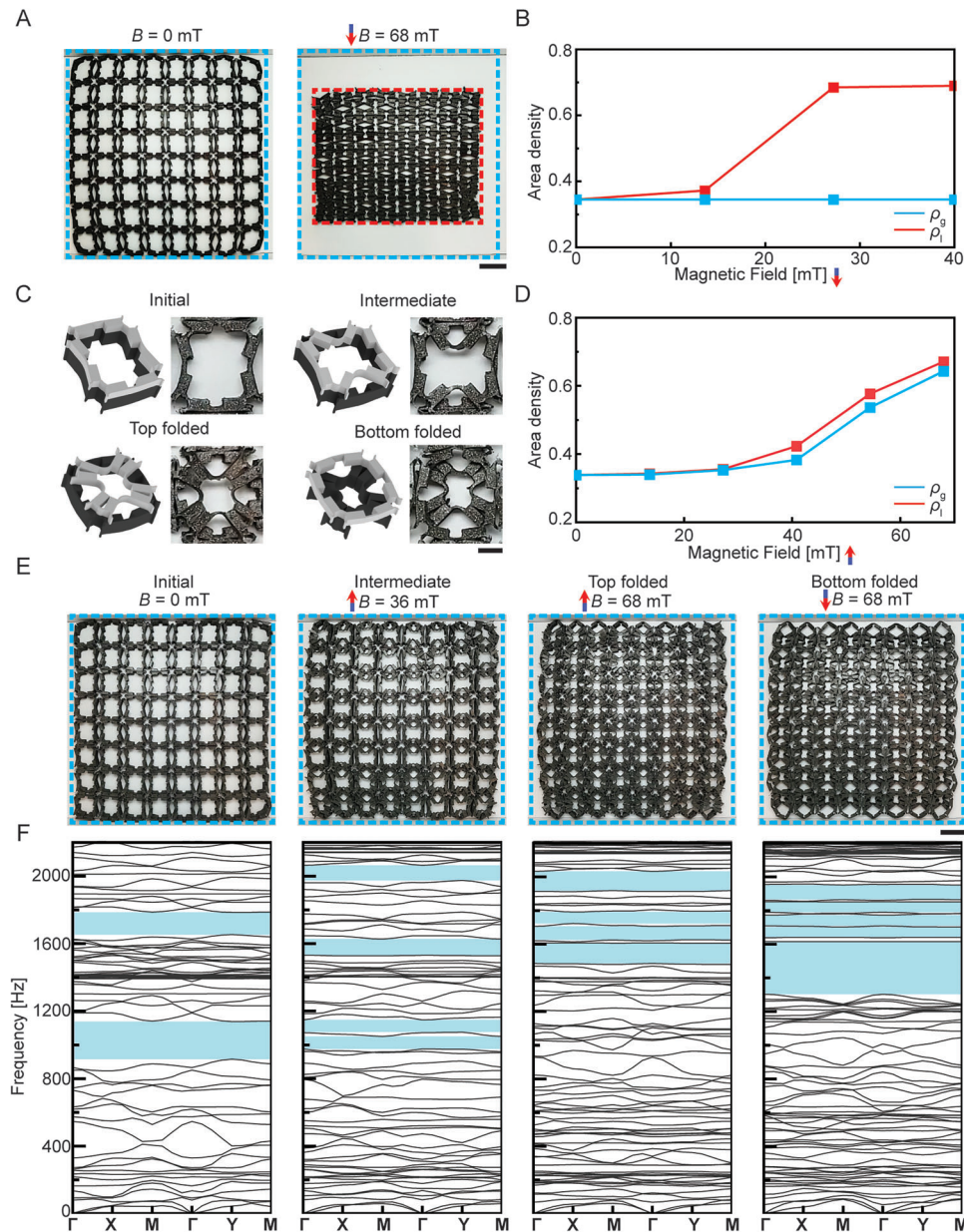


**Figure 3.** Comparison of the experimental single layer and flipped bilayer metamaterials and the acoustic bandgaps of the four deformation modes of the bilayer metamaterial. A) Magnetic actuation of the single layer metamaterial shows reduced area coverage. Scale bar: 20 mm. B) Global and local area densities of the single layer metamaterial versus downward magnetic field. C) The four modes of the flipped bilayer unit cell. Scale bar: 5 mm. D) Global and local area densities of the flipped bilayer metamaterial versus upward magnetic field. E) Four modes of magnetic actuation of the flipped bilayer metamaterial. Scale bar: 20 mm. F) Dispersion curves of modes with highlighted acoustic bandgaps at least 50 Hz wide.

and some areas along the edges of the flipped bilayer display top fold due to the inhomogeneity of the magnetic field at the edges.

Finite element analysis (FEA) is used to find the shifting acoustic bandgaps when the actuation switches among the four deformation modes, as shown in Figure 3F. The simulation utilizes the Bloch wave analysis method<sup>[51]</sup> with eigenmode calculations on the representative volume element (RVE). Details on the RVE and the Brillouin zone of the Bloch wave analysis are illustrated in Figure S8 (Supporting Information). The initial mode of the flipped bilayer exhibits two noticeable bandgaps:

914–1138 Hz and 1654–1785 Hz. At an upward 36 mT, or the intermediate mode, the first initial mode bandgap splits into two at 976–1050 Hz and 1075–1143 Hz while the second bandgap narrows and shifts to 1532–1627 Hz. A high-frequency bandgap also appears at 1974–2065 Hz for four distinct bandgaps. When the magnetic field increases to 68 mT upward, where the bilayer is in the top folded mode, four new high-frequency bandgaps appear above 1400 Hz. The first three are at 1486–1605 Hz, 1628–1706 Hz, and 1723–1791 Hz. The last bandgap is at a much higher frequency, 1919–2033 Hz. From the intermediate mode

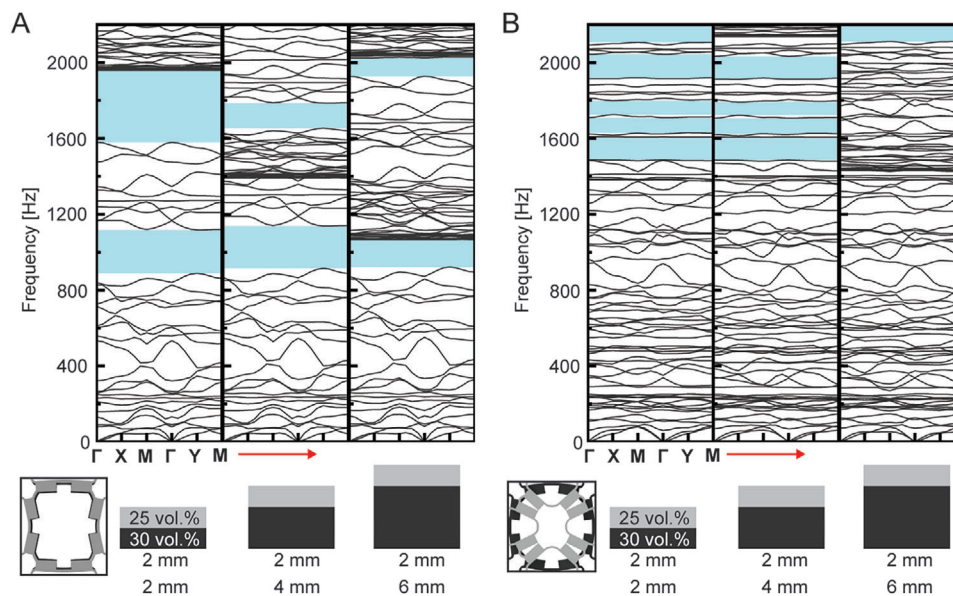


**Figure 4.** Effect of increasing bottom layer thickness on the acoustic property. The top layer has an NdFeB particle loading of 25 vol.% and the bottom layer has 30 vol.% NdFeB particles. The top layer thickness is kept constant while the bottom layer thickness increases. A) The acoustic properties of a flipped bilayer in the initial mode with bottom layer thicknesses of 2, 4, and 6 mm. B) Acoustic properties of a flipped bilayer in the top folded mode with bottom layer thicknesses of 2, 4, and 6 mm.

to the top folded mode, the low-frequency bandgaps disappear, and two additional high-frequency bandgaps appear. Then, when the 68 mT downward magnetic field is applied, the bilayer is in the bottom folded mode, and the lowest frequency bandgap widens to 1304–1616 Hz, the single widest bandgap across all modes. The next two bandgaps narrow slightly to 1641–1702 Hz and 1709–1772 Hz. Lastly, the high-frequency bandgap splits into two and shifts to 1790–1851 Hz and 1867–1951 Hz for a total of five bandgaps. Note that the acoustic property of the bottom folded mode is different from that of the top folded mode because the top and bottom layers have different thicknesses and stiffnesses due to particle loading. This is also explored as a strategy to tune acoustic performance under the same actuation mode, which is discussed in detail in the following section. Overall, the flipped bilayer shows distinct acoustic responses that can be reliably controlled through magnetic actuation. The unique combination of local area density changes, constant global dimensions, and shifting acoustic response can be used to develop highly tunable acoustic filters.

### 2.3. Parametric Study of Flipped Bilayer

In the previous section, the experimental bilayer is fabricated with an  $8 \times 8$  bottom layer of 4 mm unit cells with 30 vol.% NdFeB particles and a second  $8 \times 8$  top layer of 2 mm unit cells with 25 vol.% NdFeB particles. Since a flipped bilayer can be produced with unit cells of any thickness or particle loading, a parametric study of how unit cell thickness affects the acoustic response of a flipped bilayer is conducted, as shown in **Figure 4**. The top and bottom layers have 25 and 30 vol.% NdFeB particles, respectively. The top unit cell is kept at 2 mm, while the bottom unit cell changes thickness from 2 to 4 mm, and then, to 6 mm. In addition,

studies on layer thickness and the effect of particle loading on acoustic behavior can be found in Figures S9 and S10 (Supporting Information).

Figure 4A depicts the acoustic property modes when the flipped bilayer is in the initial mode. In each of the three presented layer thickness combinations, there are two acoustic bandgaps, but the width and location vary greatly. When both top and bottom layers are 2 mm thick, the bandgaps are located at 889–1118 Hz and 1580–1958 Hz. At a bottom thickness of 4 mm, the bandgaps shift to 915–1138 Hz and 1654–1785 Hz. At a bottom thickness of 6 mm, the bandgaps are 923–1066 Hz and 1929–2025 Hz. In all three cases, the low-frequency acoustic bandgap is very consistent and only changes slightly in its width and location. However, the high-frequency bandgap decreases in width as the bottom thickness increases. In addition, the lower limit of the bandgap increases in frequency. They can be utilized to design flipped bilayers with targeted bandgaps at certain widths and locations by using proper layer thickness.

In Figure 4B, the flipped bilayer is in the top folded mode. The first combination, 2 mm on the bottom, has five acoustic bandgaps: 1488–1606 Hz, 1630–1709 Hz, 1726–1799 Hz, 1921–2043 Hz, and 2108–2198 Hz. When the thickness of the bottom layer increases to 4 mm, the first four bandgaps display negligible changes in location and width. However, the fifth bandgap disappears altogether. Therefore, there are only four bandgaps: 1486–1605 Hz, 1628–1706 Hz, 1723–1791 Hz, and 1919–2043 Hz. When the bottom layer thickness is increased from 4 to 6 mm, all four bandgaps disappear, and the fifth bandgap that disappeared in the change from 2 to 4 mm reappears. This high-frequency bandgap is from 2112 to 2199 Hz and is close to the highest frequency bandgap when the bottom thickness equals 2 mm. Therefore, a 2D metamaterial with a thin bottom thickness will result in more acoustic bandgaps at a variety of frequency ranges in the

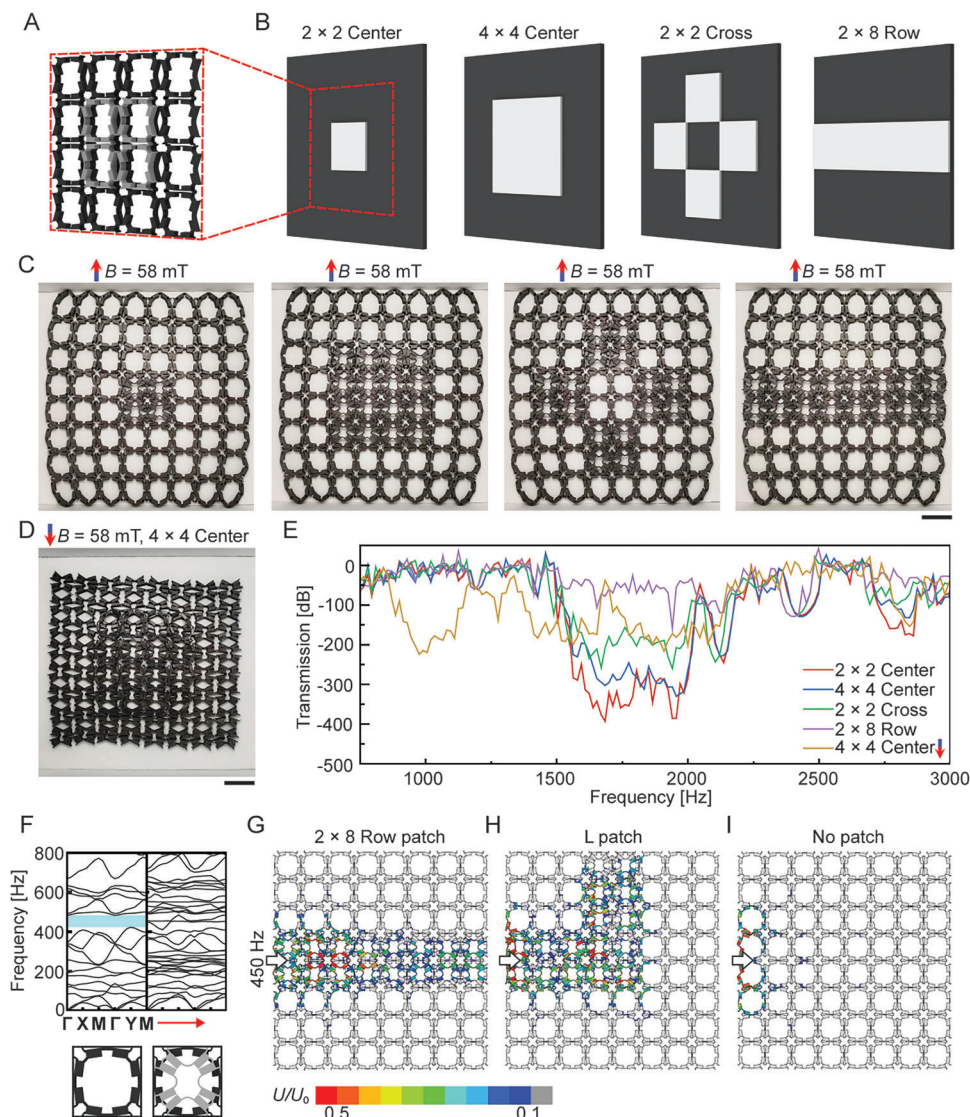


**Figure 5.** Flipped bilayer arranged in patch configurations and application as acoustic waveguides. A) A patch configuration is where the top layer has a smaller number of rows or columns than the bottom layer. B) Four patch configurations with different top layer patches of  $2 \times 2$  center,  $4 \times 4$  center,  $2 \times 2$  cross, and  $2 \times 8$  row. C) Magnetic actuation of the patch configurations where the magnetic field is 58 mT upward. D) Magnetic actuation for a  $4 \times 4$  center patch configuration under a 58 mT downward magnetic field. E) Transmission versus frequency curves of the four patch configurations when the field is 58 mT upward and the  $4 \times 4$  center when the field is 58 mT downward. F) Dispersion curves of the bottom layer in the deployed mode and the flipped bilayer in the top folded mode. G) Wave propagation along a  $2 \times 8$  row patch under a 450 Hz excitation. H) Wave propagation along an “L” patch under a 450 Hz excitation. I) No wave propagation in the bottom layer with no patch under a 450 Hz excitation. Scale bars: 20 mm.

top-folded mode. As the thickness increases, these bandgaps will disappear, while the remaining bandgaps will remain relatively unchanged. This example demonstrates the great tunability of the flipped bilayer in terms of acoustic properties.

#### 2.4. Bilayer Patch and Programmable Acoustic Waveguide

A top layer with a smaller array size can be placed on a bottom layer, like a patch, to form bilayers with much enhanced programmability. Figure 5A illustrates an example of a patch where the top layer of a  $2 \times 2$  array is stacked on a  $4 \times 4$  array bottom layer. Figure 5B shows the schematics of some sample experi-

mental flipped patch bilayers, in which all configurations have an  $8 \times 8$  bottom layer. The first configuration, called  $2 \times 2$  center, is a  $2 \times 2$  patch centered on top of the bottom layer. The second configuration is like the first but has a  $4 \times 4$  patch instead. Consequently, it is referred to as the  $4 \times 4$  center. The third patch configuration, or  $2 \times 2$  cross, utilizes four  $2 \times 2$  patches and arranges them so they form a cross with a  $2 \times 2$  void in the center. Lastly, a  $2 \times 8$  row patch is placed along the width of the bottom layer. Although we investigate the four shown configurations, there is no limit to the number of rows and columns of the top array or where it is placed. Therefore, the possible number of patch configurations and, correspondingly, property tuning ability, vastly increase.

Figure 5C and Video S4 (Supporting Information) show the magnetic actuation of the studied patch configurations. The patches are fabricated using 2 mm thick unit cells, and the bottom layers are 4 mm thick. The patch at the bottom has 30 vol.% NdFeB particles. An upward magnetic field of 58 mT actuates the patches, which can be clearly distinguished by the contracted areas. Figure 5D shows an example of a  $4 \times 4$  center patch under a downward 58 mT magnetic field. Although the magnetic field forces the top patch to remain unfolded, the unit cells directly underneath the patch fold, regardless of the magnetic attraction between the patch and bottom layer. This is due to the size difference between the two layers. The bottom layer is much larger, with a total of 64 unit cells, and only the center 16 are magnetically attracted to the patch. The remaining 48 act as a single layer and exert a large mechanical force to fold the unit cells at the center as well.

We further study how the actuation of the patches affects the acoustic transmission of the 2D metamaterials. Further information on acoustic simulation can be found in Figure S8 (Supporting Information). Figure 5E illustrates the transmission versus frequency curves of the four configurations ( $2 \times 2$  center,  $4 \times 4$  center,  $2 \times 2$  cross, and  $2 \times 8$  row) with an upward 58 mT magnetic field and the  $4 \times 4$  center under a downward 58 mT magnetic field. Here, transmission drops of at least 50 dB are considered to prevent waves from propagating. For the configurations at 58 mT upward, there are four frequency regions of interest: 1500–2015 Hz, 2045–2180 Hz, 2346–2497 Hz, and 2663–2943 Hz. In the first and fourth frequency ranges, the four configurations differ only in the depth of the transmission drop with the  $2 \times 2$  center having the deepest drop, followed by the  $4 \times 4$  center, and then the  $2 \times 2$  cross. The  $2 \times 8$  row does not exhibit any transmission drop. In the second and third frequency ranges, the four patch configurations all show the same transmission drop. At the frequencies where there are transmission drops, a single layer in the initial mode exhibits a bandgap, or deep transmission drop, and the flipped bilayer in the top folded mode does not. As more patches are added to the bottom layer, the patch configuration gradually behaves similarly to the flipped bilayer. Therefore, the  $2 \times 2$  center shows the deepest transmission drop. Although the other three patch configurations,  $4 \times 4$  center,  $2 \times 2$  cross, and  $2 \times 8$  row, have the same number of unit cells in their patches, their acoustic behavior differs because of the patch shape. The  $2 \times 2$  cross is discontinuous, and the  $2 \times 8$  row spans the entire length of the bottom layer. In comparison, the  $4 \times 4$  center at a downward 58 mT displays a different curve than the four configurations with an upward magnetic field. It has significant transmission drops at 839–1170 Hz, 1336–1683 Hz, and 1683–2150 Hz. There is also a drop in the same region as the other four configurations: 2663–2943 Hz.

Figure 5F illustrates the acoustic bandgaps for the single layer (2 mm thick, 30 vol.% NdFeB particles) in the deployed mode and the flipped bilayer (2 mm thick top layer, 4 mm thick bottom layer, both 30 vol.% NdFeB particles) in the top folded mode (see Figure S11, Supporting Information, for comparison between transmission and dispersion curves). The single layer deployed mode has a bandgap at 450 Hz, while the flipped bilayer with the top folded mode shows an all-pass behavior. Therefore, by controlling the patch path, the patch can serve as a waveguide to effectively regulate the wave propagation direction. To demonstrate this con-

cept, we simulate the wave propagation (Video S4, Supporting Information) for different patch paths at 450 Hz (see Supporting Information for details on FEA simulation). Figure 5G illustrates the wave propagation of a  $2 \times 8$  row patch configuration, illustrating the propagation of the acoustic wave as it follows the patch path along a straight line. The wave propagation in waveguide simulations shows the displacement contour normalized by the excitation amplitude,  $U/U_0$ . Figure 5H shows the wave propagation that is bent at a right angle, achieved by an L-shaped patch. Conversely, Figure 5I depicts that the acoustic wave fails to propagate in the single layer at its deployed mode because the 450 Hz wave falls into its acoustic bandgap. These examples demonstrate the viability of a patch arrangement to further expand the design space and as waveguides. Because the top layer can be easily attached or detached from the bottom layer due to the magnetic interaction, Figure 5G–I demonstrates how the bilayer patch provides a simple and flexible method to create waveguides and regulate wave propagation in 2D metamaterials.

## 2.5. Bilayer with Horizontal Offset

Another approach to overlaying two array layers into a bilayer metamaterial for effective area density tuning is the offset strategy. As shown in Figure 6A, guided by the magnetic attraction, the two array layers with the same magnetizations are automatically slightly offset when they are adhered to each other. This 2D metamaterial is called the offset bilayer. Under a downward magnetic field, both unit cells tend to fold into a compact shape. However, the constraint due to the magnetic interaction between the two layers prevents the arrays from becoming fully compacted. As a result, the unit cells transform into a cross shape. Figure 6B shows the initial and deformed configurations of a  $3 \times 3$  offset bilayer. The folded mode is noticeably smaller than the initial mode, but its dimension change is not as dramatic as the single layer. In Figure 6C, the offset bilayer consists of a top layer of 64 unit cells in an  $8 \times 8$  grid. These unit cells are 2 mm thick and contain 25 vol.% NdFeB particles. The bottom layer has the same number of unit cells as the top layer but is 4 mm thick with 30 vol.% NdFeB particles. There are three offset bilayer modes: initial, folded, and deployed. When a downward magnetic field of 68 mT is applied, the offset bilayer contracts into the folded mode (Video S5, Supporting Information). As discussed above, because of the magnetic attraction within the bilayer, the unit cells fold into a cross-like shape. An upward magnetic field of 68 mT expands the offset bilayer into the deployed mode. Figure 6D shows the area densities of the offset bilayer under the downward magnetic field. Because of the offset array arrangement, both the global and local area densities increase during actuation, showing an improving, but not perfect, area-preserving actuation compared to the actuation of the single layer. The complete area densities in both magnetic field directions are shown in Figure S12 (Supporting Information). Figure 6E depicts the acoustic transmission versus frequency curves of the offset bilayer. In the first and second frequency regions, 988–1155 Hz and 1336–1638 Hz, only the folded mode shows significant transmission drops. However, for the third frequency region, the offset bilayer in the folded mode does not show any transmission drops, and the deployed mode shows a transmission drop of 447 dB



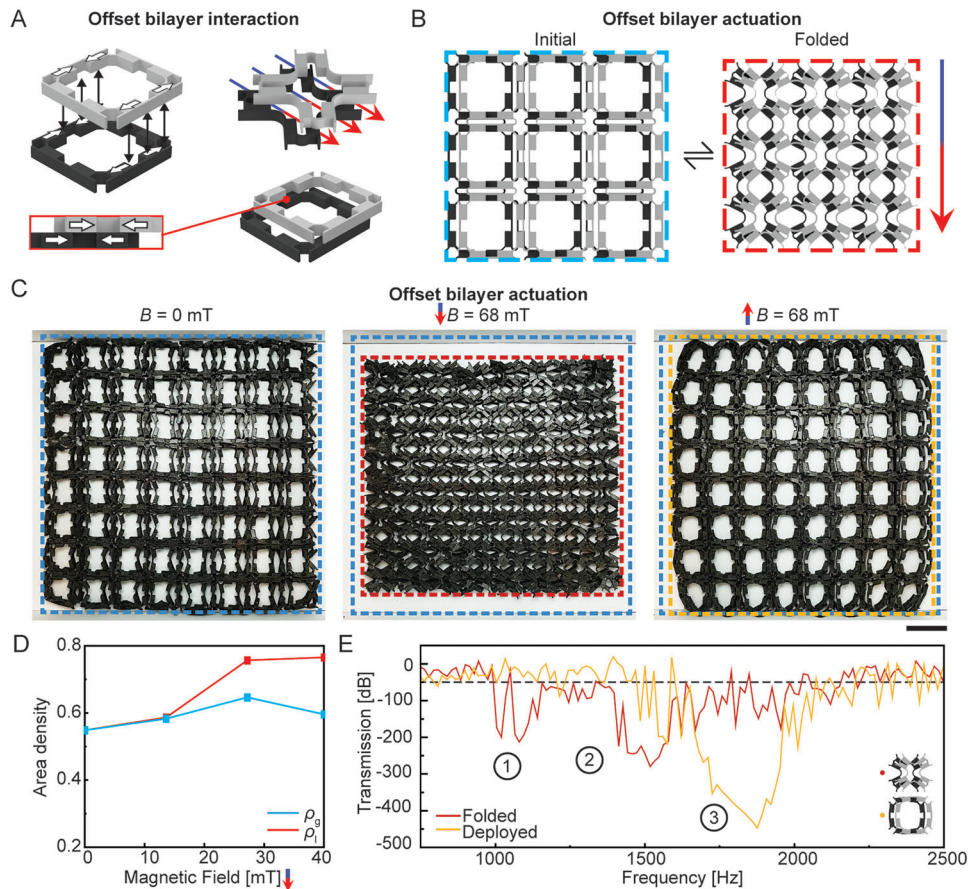


**Figure 6.** Offset bilayer metamaterial. A) Magnetic interaction between two unit cells arranged in an offset bilayer. B) A  $3 \times 3$  offset bilayer and its magnetic actuation. C) Actuation of the experimental offset bilayer. Scale bar: 20 mm. D) Global and local area densities of the offset bilayer metamaterial versus downward magnetic field. E) Acoustic transmission versus frequency curves of the offset bilayer in the folded and deployed modes.

from 1650 to 2071 Hz. Therefore, the offset bilayer can be utilized as a device for switchable acoustic bandgaps, where two low-frequency bandgaps are switched for a high-frequency bandgap via a magnetic field.

### 3. Conclusion

We report magneto-mechanical bilayer metamaterials that achieve excellent shape and property tunability through a novel strategy where the unit cells are arranged in double-layer patterns. This new design method allows for the 2D metamaterials to adjust their area densities with negligible change to their overall dimensions. We presented three bilayer strategies: flipped bilayer, patch configurations, and offset bilayer. The flipped bilayer utilizes separate actuation of its two layers to achieve increased shape transformations, property tunability, and exceptional area preservation. The patch configuration greatly expands the design space and can be utilized as a reconfigurable waveguide. The offset bilayer also shows improved area preservation and property tunability. These novel strategies utilizing two layers to simultaneously achieve shape deformation and area preservation offer immense potential for new 2D metamaterials with better property controllability. Their area-preserving capability and exceptional tunability in the switching of bandgap modes allow

for practical applications in vibration isolation and cloaking. The patch-assembling strategy also demonstrates the efficacy of the 2D metamaterial in guiding wave propagation. In this work, the unit cells of the 2D metamaterial entirely consist of a soft polymer embedded with hard magnetic particles. However, the design extends beyond soft materials and can be implemented using more rigid blocks and soft hinges that permit the same structural deformation response to a magnetic field. But because a more rigid metamaterial will consist of two different material types, the wave propagation will vastly differ, warranting further study. The design of the magneto-mechanical 2D metamaterial can be further guided by machine learning methods for optimized structural design<sup>[43]</sup> and actuation programming to achieve desired property tunability. In addition, the actuation of magneto-mechanical 2D metamaterials is not limited to the use of large electromagnetic coils. Permanent magnets can be used to induce a magnetic field, which can be used to apply local magnetic fields to specific portions of the metamaterial. Furthermore, there are methods to lock the deformation mode of the bilayer metamaterials such that the metamaterial remains deformed even in the absence of a magnetic field. For example, magnetic shape memory polymers (M-SMPs)<sup>[49]</sup> can either stiffen or soften in response to temperature, providing shape locking and unlocking. The reported magneto-mechanical bilayer 2D metamaterials

open exciting possibilities for using structural reconfiguration for wave manipulation without changing the overall dimensions of the system. We envision that not only will these metamaterials bring new acoustic applications but also other types of wave control, such as electromagnetic filters with highly tunable frequencies.

## 4. Experimental Section

**Unit Cell Preparation:** In this study, three different unit cells were used to create 2D metamaterials. In all three cases, Dragon Skin 20 (Smooth-On Inc., Macungie, PA, USA) and NdFeB particles (average particle size of 100  $\mu\text{m}$ , Magnequench, Singapore) were mixed, degassed, and injected into polyvinyl alcohol (PVA) molds 3D-printed with an Ultimaker S5 (Ultimaker, Netherlands). The filled molds were covered with a glass slide, and the material was cured at 80  $^{\circ}\text{C}$  for 1 h. PVA is flexible at high temperatures, allowing the cured unit cells to be removed easily. The first unit cell was 4 mm thick and had a particle loading of 30 vol.%. The other two unit cells were both 2 mm thick with 25 and 30 vol.% NdFeB particles, respectively. To achieve the magnetization shown in Figure 1A, the unit cells were deformed into a “diamond” shape and held in place with a 3D-printed polylactic acid (PLA) fixture. This mold was placed in a homemade coil and magnetized under a 1.5 T magnetic impulse field. Figures S1 and S2 (Supporting Information) include further information regarding the dimensions and fabrication process of the unit cell.

**2D Metamaterial Array Fabrication:** After magnetization, the unit cells were placed into a 3D-printed PLA fixture that allowed the hinges of each unit cell to touch. The hinges were connected using Sil-poxy adhesive (Smooth-On Inc., Macungie, PA, USA). The unit cells were removed from the fixture after the adhesive was allowed to cure at room temperature for 12 min.

**Acoustic Simulation:** The acoustic properties of each deformation mode in all 2D metamaterials were predicted using the commercial software ABAQUS 2021 (Dassault Systèmes SE, Vélizy-Villacoublay, France) and COMSOL Multiphysics 5.5 (COMSOL Inc., Stockholm, Sweden). A steady state dynamic analysis in ABAQUS was performed on 2D metamaterials with non-periodic structures such as the patch bilayer and offset bilayer for transmission-frequency curves. A dynamic, explicit step was used for the waveguide simulations. Bloch wave analysis was carried out to predict the flipped bilayer bandgaps using COMSOL eigenfrequency analysis. More simulation details are provided in the Supporting Information.

**Experimental Setup:** The 2D metamaterials were positioned between two Helmholtz coils, spaced 150 mm apart. The coils were connected to a 4700  $\mu\text{F}$  capacitor powered at 120 V. The magnetic field between the coils was controlled by adjusting the current delivered to the coils using a MATLAB script. Further information on the experimental setup can be found in the Supporting Information.

**Material Characterization:** Dragon Skin 20 and NdFeB particles were mixed into a homogenous mixture in specific volume percentages and degassed. The mixture was then poured into acrylic molds for tensile test specimens. The filled molds were then cured in an oven at 80  $^{\circ}\text{C}$  for 1 h, and the molds were removed from the test specimens. An Instron 3344 (Instron Corp., Norwood, MA, USA) was used to characterize the displacement versus force data to obtain the shear modulus. Three specimens were tested for particle loadings of 20, 25, and 30 vol.%, with averaged Young's moduli of 1.15, 1.77, and 2.64 MPa, respectively. The densities of the mixtures were calculated using the given densities of the NdFeB particles and Dragon Skin 20. More information on the material characterization can be found in the Supporting Information.

**Area Density Calculation:** Actuation videos were recorded of the fabricated 2D metamaterials placed inside the magnetic coils and actuated at specific magnetic fields. Image analysis of the 2D metamaterials was conducted by cropping image snapshots of the videos and calculating the total number of pixels in  $A_{\text{meta}}$ ,  $A_{\text{initial}}$ , and  $A_{\text{deform}}$ , and then calculating the global and local area densities.

## Supporting Information

Supporting Information is available from the Wiley Online Library or from the author.

## Acknowledgements

The authors acknowledge the support from NSF Career Award CMMI-2145601 and NSF Award CMMI-2142789.

## Conflict of Interest

The authors declare no conflict of interest.

## Author Contributions

R.R.Z. designed the research. J.S., S.W., and J.D. performed the research. J.S. and J.D. carried out the experiments and analyzed the data. S.W. realized the FEA simulations. All authors wrote the paper.

## Data Availability Statement

The data that support the findings of this study are available from the corresponding author upon reasonable request.

## Keywords

acoustic bandgaps, acoustic waveguides, active metamaterials, magnetic actuation, multimodal deformation

Received: April 17, 2023  
Revised: June 5, 2023  
Published online:

- [1] T. Chen, M. Pauly, P. M. Reis, *Nature* **2021**, 589, 386.
- [2] T. Li, F. Liu, L. Wang, *Compos. Part B Eng.* **2020**, 198, 108229.
- [3] D. Neshev, I. Aharonovich, *Light Sci. Appl.* **2018**, 7, 58.
- [4] E. W. Wang, T. Phan, S. J. Yu, S. Dhuey, J. A. Fan, *Proc. Natl. Acad. Sci. USA* **2022**, 119, e2122085119.
- [5] A. E. Forte, D. Melancon, M. Zanati, M. De Giorgi, K. Bertoldi, *Adv. Funct. Mater.* **2023**, 33, 2214897.
- [6] Y. Zhang, X. Yang, J. Gao, *Sci. Rep.* **2018**, 8, 4884.
- [7] K. Chen, G. Ding, G. Hu, Z. Jin, J. Zhao, Y. Feng, T. Jiang, A. Alù, C. W. Qiu, *Adv. Mater.* **2020**, 32, 1906352.
- [8] Z. Li, J. Liu, J. Zhang, L. Shao, C. Zhang, X. Wang, R. Jin, W. Zhu, *Adv. Mater. Technol.* **2022**, 7, 1.
- [9] M. Boyarsky, T. Sleasman, M. F. Imani, J. N. Gollub, D. R. Smith, *Sci. Rep.* **2021**, 11, 4693.
- [10] Q. Huang, L. T. Gan, J. A. Fan, *Adv. Mater.* **2023**, 35, 2204688.
- [11] S. Wu, J. Eichenberger, J. Dai, Y. Chang, N. Ghalichechian, R. R. Zhao, *Adv. Intell. Syst.* **2022**, 4, 2200106.
- [12] O. R. Bilal, A. Foehr, C. Daraio, *J. Appl. Mech. Trans. ASME* **2020**, 87, 071009.
- [13] F. Javid, P. Wang, A. Shanian, K. Bertoldi, *Adv. Mater.* **2016**, 28, 5943.
- [14] Z. Jia, Y. Chen, H. Yang, L. Wang, *Phys. Rev. Appl.* **2018**, 9, 44021.
- [15] L. Tong, Z. Xiong, Y. X. Shen, Y. G. Peng, X. Y. Huang, L. Ye, M. Tang, F. Y. Cai, H. R. Zheng, J. Bin Xu, G. J. Cheng, X. F. Zhu, *Adv. Mater.* **2020**, 32, 1.

- [16] H. Zhu, T. F. Walsh, F. Semperlotti, *Appl. Phys. Lett.* **2018**, *113*, 221903.
- [17] B. Liang, J. C. Cheng, C. W. Qiu, *Nanophotonics* **2018**, *7*, 1191.
- [18] H. T. Zhou, W. X. Fu, Y. F. Wang, Y. S. Wang, V. Laude, C. Zhang, *Mater. Des.* **2021**, *199*, 109414.
- [19] Y. Xue, X. Zhang, *Extrem. Mech. Lett.* **2021**, *46*, 101347.
- [20] J. J. Park, J.-H. Kwak, K. Song, *Extrem. Mech. Lett.* **2021**, *43*, 101203.
- [21] E. Bok, J. J. Park, H. Choi, C. K. Han, O. B. Wright, S. H. Lee, *Phys. Rev. Lett.* **2018**, *120*, 44302.
- [22] C. Shen, Y. Xie, J. Li, S. A. Cummer, Y. Jing, *Appl. Phys. Lett.* **2016**, *108*, 2.
- [23] Y. Li, B. M. Assouar, *Appl. Phys. Lett.* **2016**, *108*, 063502.
- [24] X. Guo, V. E. Gusev, V. Tournat, B. Deng, K. Bertoldi, *Phys. Rev. E* **2019**, *99*, 052209.
- [25] Z. Tian, C. Shen, J. Li, E. Reit, Y. Gu, H. Fu, S. A. Cummer, T. J. Huang, *Adv. Funct. Mater.* **2019**, *29*, 1808489.
- [26] O. R. Bilal, A. Foehr, C. Daraio, *Adv. Mater.* **2017**, *29*, 1.
- [27] N. Gao, S. Qu, L. Si, J. Wang, W. Chen, *Appl. Phys. Lett.* **2021**, *118*, 063502.
- [28] S. M. Montgomery, S. Wu, X. Kuang, C. D. Armstrong, C. Zemelka, Q. Ze, R. Zhang, R. Zhao, H. J. Qi, *Adv. Funct. Mater.* **2021**, *31*, 2005319.
- [29] P. Cao, Y. Zhang, S. Zhang, W. Ou, S. G. Mosanenzadeh, N. X. Fang, *Phys. Rev. Appl.* **2020**, *13*, 1.
- [30] X. Fang, J. Wen, L. Cheng, D. Yu, H. Zhang, P. Gumbsch, *Nat. Mater.* **2022**, *21*, 869.
- [31] J. B. Reeves, R. K. Jayne, T. J. Stark, L. K. Barrett, A. E. White, D. J. Bishop, *Nano Lett.* **2018**, *18*, 2802.
- [32] A. G. Izard, L. Valdevit, *Adv. Eng. Mater.* **2020**, *22*, 1901019.
- [33] B. Li, C. Zhang, F. Peng, W. Wang, B. D. Vogt, K. T. Tan, *J. Mater. Chem. C* **2021**, *9*, 1164.
- [34] Z. Zhao, C. Yuan, M. Lei, L. Yang, Q. Zhang, H. Chen, H. J. Qi, D. Fang, *Phys. Rev. Appl.* **2019**, *11*, 1.
- [35] Z. Hu, Z. Wei, K. Wang, Y. Chen, R. Zhu, G. Huang, G. Hu, *Nat. Commun.* **2023**, *14*, 1266.
- [36] X. Peng, S. Wu, X. Sun, L. Yue, S. M. Montgomery, F. Demoly, K. Zhou, R. R. Zhao, H. J. Qi, *Adv. Mater.* **2022**, *34*, 1.
- [37] Y. Chen, X. Li, H. Nassar, G. Hu, G. Huang, *Smart Mater. Struct.* **2018**, *27*, 115011.
- [38] Y. Chen, X. Li, G. Hu, M. R. Haberman, G. Huang, *Nat. Commun.* **2020**, *11*, 3681.
- [39] E. Arbabi, A. Arbabi, S. M. Kamali, Y. Horie, M. S. Faraji-Dana, A. Faraon, *Nat. Commun.* **2018**, *9*, 812.
- [40] Z. Alameh, S. Yang, Q. Deng, P. Sharma, *Soft Matter* **2018**, *14*, 5856.
- [41] Y. Chen, Q. Liang, C. Y. Ji, X. Liu, R. Wang, J. Li, *J. Appl. Phys.* **2022**, *131*, 233102.
- [42] Q. Zhang, A. V. Cherkasov, N. Arora, G. Hu, S. Rudykh, *Extrem. Mech. Lett.* **2023**, *59*, 101957.
- [43] C. Ma, Y. Chang, S. Wu, R. R. Zhao, *ACS Appl. Mater. Interfaces* **2022**, *14*, 33892.
- [44] C. Ma, S. Wu, Q. Ze, X. Kuang, R. Zhang, H. J. Qi, R. Zhao, *ACS Appl. Mater. Interfaces* **2021**, *13*, 12639.
- [45] R. Zhao, Y. Kim, S. A. Chester, P. Sharma, X. Zhao, *J. Mech. Phys. Solids* **2019**, *124*, 244.
- [46] T. Jiralerspong, G. Bae, J. H. Lee, S. K. Kim, *ACS Nano* **2020**, *14*, 17589.
- [47] Y. Kim, H. Yuk, R. Zhao, S. A. Chester, X. Zhao, *Nature* **2018**, *558*, 274.
- [48] Y. Alapan, A. C. Karacakol, S. N. Guzelhan, I. Isik, M. Sitti, *Sci. Adv.* **2020**, *6*, abc6414.
- [49] Q. Ze, X. Kuang, S. Wu, J. Wong, S. M. Montgomery, R. Zhang, J. M. Kovitz, F. Yang, H. J. Qi, R. Zhao, *Adv. Mater.* **2020**, *32*, 1906657.
- [50] S. Wu, Q. Ze, R. Zhang, N. Hu, Y. Cheng, F. Yang, R. Zhao, *ACS Appl. Mater. Interfaces* **2019**, *11*, 41649.
- [51] M. Åberg, P. Gudmundson, *J. Acoust. Soc. Am.* **1997**, *102*, 2007.